

Cite this: DOI: 00.0000/xxxxxxxxxx

Characterizing the free-energy landscapes of DNA origamis[†]

Chak Kui Wong,^a Chuyan Tang,^a John S. Schreck,^b and Jonathan P. K. Doye^{*a}

Received Date

Accepted Date

DOI: 00.0000/xxxxxxxxxx

We show how coarse-grained modelling combined with umbrella sampling using distance-based order parameters can be applied to compute the free-energy landscapes associated with mechanical deformations of large DNA nanostructures. We illustrate this approach for the strong bending of DNA nanotubes and the potentially bistable landscape of twisted DNA origami sheets. The homogeneous bending of the DNA nanotubes is well described by the worm-like chain model; for more extreme bending the nanotubes reversibly buckle with the bending deformations localized at one or two “kinks”. For a twisted one-layer DNA origami, the twist is coupled to the bending of the sheet giving rise to a free-energy landscape that has two nearly-degenerate minima that have opposite curvatures. By contrast, for a two-layer origami, the increased stiffness with respect to bending leads to a landscape with a single free-energy minimum that has a saddle-like geometry. The ability to compute such landscapes is likely to be particularly useful for DNA mechanotechnology and for understanding stress accumulation during the self-assembly of origamis into higher-order structures.

1 Introduction

DNA nanotechnology aims to design and construct self-assembled nanoscale DNA structures through utilizing the specificity of Watson-Crick base-pairing and the structural rigidity of the DNA double helix^{1,2}. Probably the most commonly used method is DNA origami^{3,4}. In this method, a long viral DNA single strand, often termed the “scaffold” strand, is folded into the target structure with the aid of many different “staple” strands that are programmed to hybridize to multiple specific domains of the scaffold strand.

Probably the most basic property of a DNA origami is its equilibrium average structure and the thermal fluctuations about that average. The most detailed experimental views of origami structure can be obtained from cryo-EM studies^{5,6} with lower-resolution imaging available from TEM and AFM. Alternatively, computer modelling can be used to gain structural insights into DNA nanostructures. All-atom molecular dynamics simulations can provide the highest level of detail^{7–12}, but are computationally very expensive because of the large size of DNA origamis. On the other hand, coarse-grained models such as oxDNA^{13–15},

mrDNA¹⁶, CanDo^{17,18} and SNUPI¹⁹ provide a lower level of detail, but are computationally much less expensive and so can be routinely used to gain insight into origami structure^{20,21}, even for those that are very flexible and diffusively explore their configuration space^{22–26}.

The free-energy landscapes associated with more extreme fluctuations are also potentially important. For example, such landscapes can describe the response of DNA origami to stresses, and so are particularly pertinent to the field of DNA mechanotechnology²⁷ that uses DNA nanodevices to sense²⁸ or apply forces,^{29,30} and to origamis in which internal stresses are used to modulate the structure.^{31–34} Furthermore, for origamis with multiple stable states,^{35–37} the landscapes would allow the mechanisms of interconversion and the free-energy barriers between the states to be characterized. Additionally, for origamis that are designed to assemble into higher-order structures, the monomer landscapes could help predict the thermodynamics of stress accumulation, particularly for examples where the stress accumulation is a design feature, for example, to make the assembly self-limiting.^{38,39}

One of the most common methods for computing free-energy landscapes is umbrella sampling⁴⁰, in which a bias is applied during the simulations to allow sampling of high free-energy conformations. For example, for small DNA systems it has been used to study processes such as stacking^{41,42}, condensation^{43,44}, and unwinding⁴⁵ in all-atom detail. Coarse-grained models allow this approach to be applied to larger systems and slower processes. For example, the oxDNA model has been used to study the free-energy landscapes for a wide variety of processes involving assembly and/or mechanical deformation both for basic DNA mo-

^a Physical and Theoretical Chemistry Laboratory, Department of Chemistry, University of Oxford, South Parks Road, Oxford, OX1 3QZ, UK. E-mail: jonathan.doye@chem.ox.ac.uk

^b National Center for Atmospheric Research, Computational and Information Systems Laboratory, 850 Table Mesa Drive, Boulder, CO 80305, USA

[†] Electronic Supplementary Information (ESI) available: Further details of simulation methods, additional supporting results and animations. See DOI: 00.0000/00000000.

tifs^{46–48} and for small DNA nanodevices.^{49–51}

Here, we apply this approach to sample some example free-energy landscapes associated with full-size origamis. Such calculations, although computationally expensive, are feasible both because we are using a coarse-grained model (oxDNA) and because we are considering the free-energy landscapes for structural variables where equilibration mainly involves relatively fast processes associated with mechanical relaxation rather than slow processes such as hybridization.

The first example we consider is the bending and stretching of DNA nanotubes⁵² under external stress. One might expect that the behaviour will be somewhat analogous to that for double-stranded DNA. When weakly bent, duplex DNA can be described with the worm-like chain (WLC) model,⁵³ but under strong bending, its behaviour deviates from the model due to localized buckling to form a kink that typically involves broken base pairs.^{54–56} Previous analysis of such nanotubes have shown that the WLC model provides a good description of their thermal fluctuations,⁵⁷ but it will be interesting to explore the degree of bending that can be achieved before kink formation, the structure of the kinks that form and whether such buckling leads to irreversible damage to the nanotubes.

In the second example we consider the coupling between twist and curvature in twisted origami sheets. For an inextensible sheet, twist must lead to curvature, where there are two possible states that differ in the sign of the curvature and the diagonal about which bending occurs. That such single-layer DNA origami sheets exhibit curvature has been confirmed by SAXS⁵⁸ and cryoEM⁶; AFM studies have also attempted to identify the preferred direction of curvature.^{35,59} Here, we characterize the free-energy landscapes of twisted DNA origami sheets to probe whether there are indeed two free-energy minima; we also explore the effects of sheet thickness on this potential bistability.

To compute these free-energy landscapes we use oxDNA, which is a coarse-grained model of DNA at the nucleotide level.^{13–15} It has been designed to reproduce the structure, thermodynamics and mechanics of double- and single-stranded DNA. This allows it to capture many biophysical properties of DNA;⁶⁰ those particularly relevant to the current study include the response of double-stranded DNA to bending stress^{46,56} and the fraying or breaking of DNA base-pairs under stress more generally.⁴⁷ Moreover, the latest version of the model is able to accurately model the structural properties of DNA origami,²⁰ and so has been applied to study a wide range of different types of DNA origami.^{21–23,38,61} Given the above, we are confident in using oxDNA to calculate the free-energy landscapes for our chosen DNA origamis, as detailed in the rest of this article.

2 Methods

To model the DNA nanostructures we use the oxDNA coarse-grained model.^{13–15} In the oxDNA model, each nucleotide is represented by a rigid body. The nucleotides interact through a pairwise potential which has terms representing backbone connectivity, excluded-volume interactions, hydrogen bonding between base pairs, stacking interactions, and electrostatic interactions between backbone phosphate groups. Solvent is modelled implicitly

as a dielectric continuum, and we choose to use a salt concentration of $[\text{Na}^+] = 1.0 \text{ M}$, which is representative of the high salt conditions typically used for DNA nanotechnology. Although this simple approach to DNA electrostatics has been shown to overestimate interhelical repulsions,⁶² at these high salt concentrations (and short Debye screening lengths) we do not expect any inaccuracies to significantly affect the results.

The oxDNA simulation code was used to perform molecular dynamics simulations in the canonical ensemble, in particular making use of its GPU implementation.⁶³ In the umbrella sampling simulations, harmonic biasing potentials in the order parameters were placed at the centre of each window. The free-energy landscapes were constructed from the order-parameter probability distributions for each window using the weighted-histogram analysis method (WHAM).⁶⁴ For the 1D umbrella sampling of the DNA nanotubes 500 windows were used, and in the 2D umbrella sampling of the origami sheets 10 000 windows were used. We iterated the sets of umbrella sampling simulations until the WHAM-generated landscapes no longer changed.

Additional simulation and analysis details can be found in the Supplementary Information.

3 Results and Discussion

3.1 DNA nanotube mechanics

The DNA nanotubes that we study here are all six-helix bundles with a hexagonal cross-section. Six-helix bundles have been particularly well characterized^{6,65–67}, and commonly used — example applications include as chiral liquid-crystal mesogens⁶⁸ and stiff handles for force spectroscopy.⁶⁹ For two of the examples studied here, the elastic mechanical properties have been measured experimentally^{65,69}. First, we consider the general properties of the free-energy landscapes that describe the nanotube bending by considering a single example, before focusing on how the details of the designs can affect these properties.

To describe the degree of bending, we define an end-to-end distance R_{ee} for the nanotubes (Fig. 1(a)). This “order parameter” is then used to bias the systems to sample extremely bent states. The umbrella sampling works by running multiple simulations each of which samples a different R_{ee} “window” by adding a harmonic “umbrella” potential that constrains R_{ee} to be near to the minimum of that particular potential. A best estimate of the probability distribution $p(R_{ee})$ can then be reconstructed from the distributions in the individual simulations. The free-energy landscape is then simply $A(R_{ee}) = -k_B T \log(p(R_{ee})) + c$ where we choose c such that the free-energy global minimum has a value of 0.

The free-energy landscape that results from this “1-dimensional” umbrella sampling is shown in Fig. 1(b) for the six-helix bundle studied in Ref. 65 along with some representative configurations at different R_{ee} in Fig. 1(a) and (c). The landscape has a minimum close to the contour length of the nanotube; this minimum is asymmetric as it costs more to extend R_{ee} by stretching the nanotube than to reduce R_{ee} by bending the nanotube. That being said the nanotube is still extremely stiff towards bending; for example, it costs more than $100 k_B T$ to reduce R_{ee} by 50%.

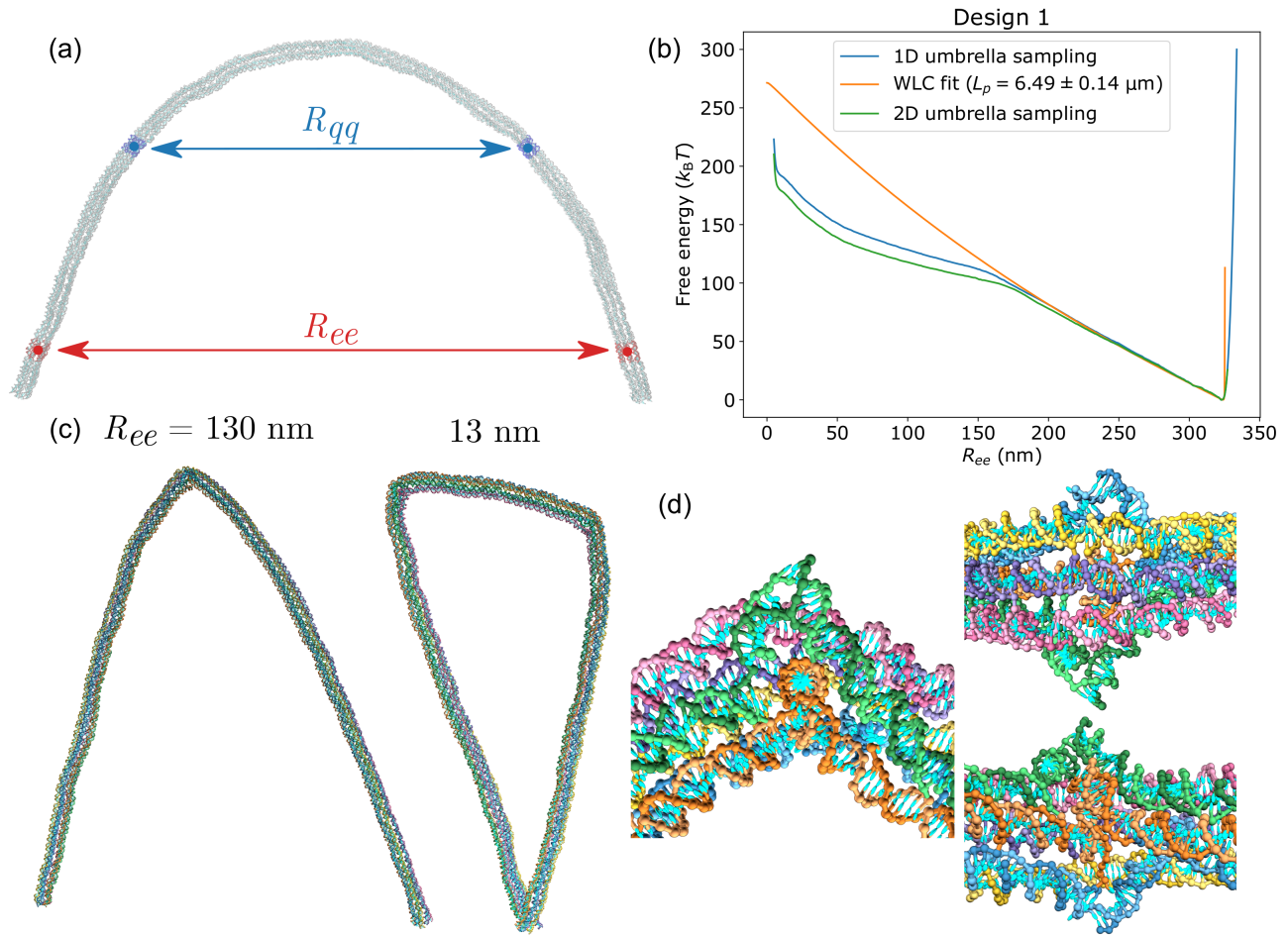


Fig. 1 (a) The end-to-end distance R_{ee} and the $\frac{1}{2}$ - $\frac{1}{2}$ distance R_{qq} that are used as order parameters in the umbrella sampling illustrated for the design 1 nanotube with $R_{ee} = 210$ nm. Each distance is defined with respect to the centres of mass of the shaded sets of nucleotides. As the helices at the ends of an origami tend to splay out more, we use sets of nucleotides slightly in from the ends to define R_{ee} . (b) Free-energy landscape of design 1 as a function of R_{ee} computed by 1- and 2-dimensional umbrella sampling. The weak-bending regime of the landscape can be fitted to the WLC model (see Table S2 for the fitting parameters). (c) Further representative configurations at different R_{ee} . (d) Close-ups of the kink for the $R_{ee} = 130$ nm configuration. Views are from the side, outside and inside of the kink.

The landscape has a clear change in slope at about 160 nm that corresponds to the onset of “kink” formation, where it becomes more favourable to localize much of the stress at a defect rather than the system being homogeneously bent. Finally, there is a sharp rise in the free-energy as R_{ee} approaches zero because the nucleotides at the two ends then begin to overlap.

In the weak to moderate bending regime, we expect the behaviour of the nanotube to be well described by the WLC model. Indeed, the fit to the free-energy landscape in this regime using the WLC formula for $p(R_{ee})$ given in Ref. 70 accurately describes the landscape up until the onset of kink formation. Note that this is despite significant local inhomogeneities in the nanotube; for example, bending of the individual helices at nicks and junctions is likely to be somewhat easier, and the relative motion of the helices is much more tightly constrained at junctions. As observed in Ref. 57, although these inhomogeneities lead to significant deviations from worm-like chain behaviour at short length scales, as longer length scales are considered the nanotubes behave more and more like an ideal worm-like chain. Note also that the WLC

form cannot capture the behaviour of the landscape when R_{ee} is larger than that for the free-energy minimum, i.e. when the nanotube is stretched; this is simply because the formula is for the standard form of the WLC model which assumes the “chain” is inextensible.

In the strong bending regime, a kink develops in the nanotube, which leads to deviation from WLC behaviour. The formation of the kink can be caused by the localization of the bending stress in a small region in order to relieve the bending stress in the rest of nanotube. Generally, the kink occurs near to the centre of the nanotube as this is most effective at bringing the two ends of the nanotube close, however the exact position varies between individual simulations. A close-up of a kink is shown in Fig. 1(d). Helices in the outer part of the kink are stretched, while those in the inner part are compressed and forced out of the helical axis. At very small R_{ee} it can become favourable for the nanotube to adopt a configuration with two kinks with bend angles of near to 90° rather than a configuration with a single kink with a bend angle near to 180° .

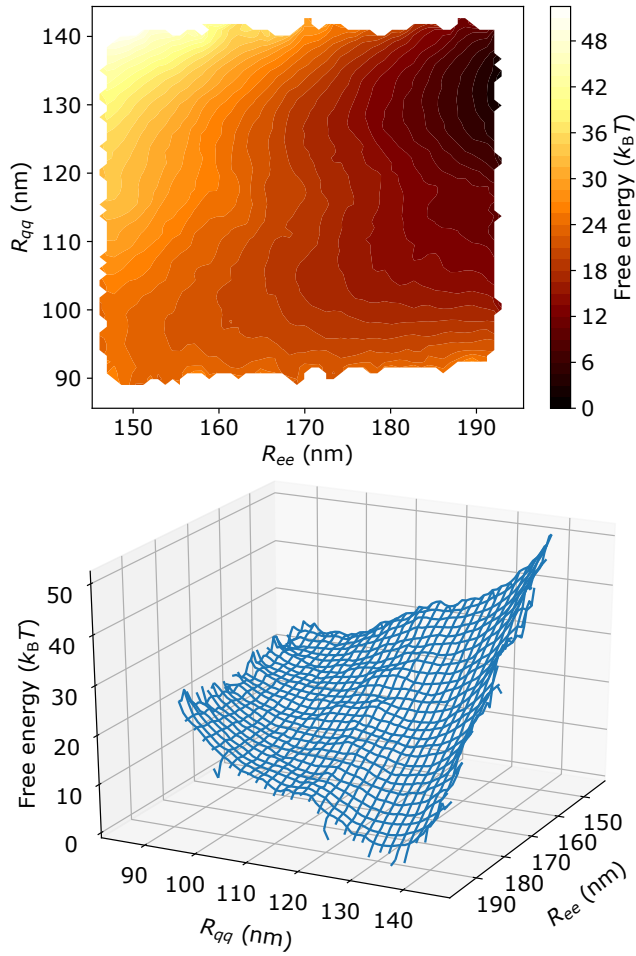


Fig. 2 Two-dimensional free-energy landscape of design 1 as a function of R_{ee} and R_{qq} . The two plots provide two different representations of the same landscape.

The relative smoothness of the free-energy landscape in the two regimes is indicative that the landscape is well sampled in these regimes. However, accurately locating the point at which the crossover between the two regimes occurs is more challenging, because kink formation and resolution are relatively slow processes on the simulation time scales. One reason for this slowness is that kink formation is coupled to global shape changes of the nanotube. For example, the potential benefit of introducing a kink at the centre of a homogeneously bent configuration like that in Fig. 1(a) is only felt once the bending in the rest of the nanotube relaxes and the arms on either side of the kink become relatively straight.

One way to aid the sampling in such cases is to perform two-dimensional umbrella sampling where a second order parameter is introduced that can differentiate between the two forms. The order parameter that we introduce is R_{qq} the distance between points one quarter and three quarters along the nanotube; for a given R_{ee} this should have a smaller value in the kinked states because the nanotube sections either side of the kink are relatively straight. Furthermore, this order parameter directly facilitates the global shape changes to which kink formation is coupled. For ex-

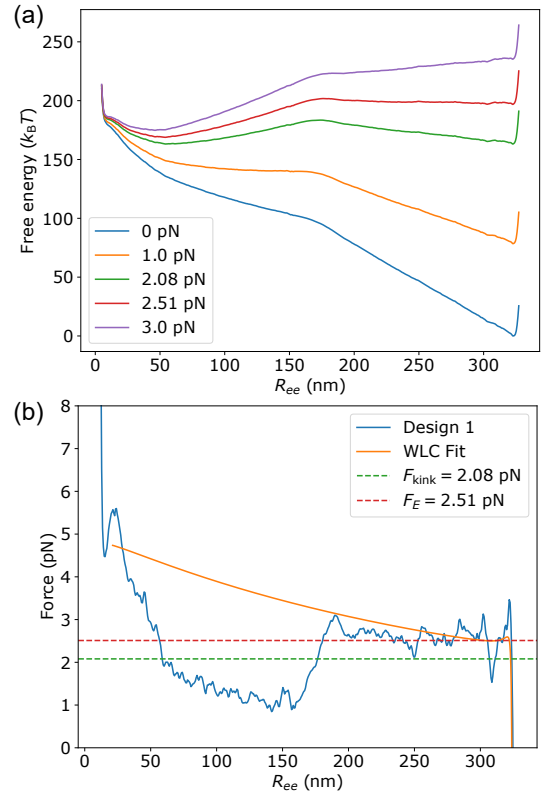


Fig. 3 (a) The free-energy landscape for the design 1 nanotube at a series of compressive forces along the end-to-end vector, where $A(R_{ee}; F) = A(R_{ee}) + FR_{ee}$. (b) $F(R_{ee}) = -dA(R_{ee})/dR_{ee}$ for the computed landscape and its WLC fit. The two horizontal lines correspond to the force at which the two free-energy minima associated with the kinked and unkinked states are degenerate and the predicted Euler buckling critical force. Note that the noise in the force curve is due to a certain small degree of roughness in the simulation-derived landscapes.

ample, decreasing R_{qq} for the configuration in Fig. 1(a) will begin to localize the bending in the centre of nanotube and straighten the sections either side.

The resulting two-dimensional free-energy landscape is shown in Fig. 2 for the transition region. It has two clear valleys corresponding to the kinked and homogeneously bent states, the latter having a steeper gradient. At intermediate values of R_{ee} cuts through the landscape have two minima separated by a barrier as a function of R_{qq} . Such a cut is illustrated in Fig. S5 at an R_{ee} value near to the centre of the kink transition along with representative configurations.

Combining the information from the two-dimensional umbrella sampling in the transition region with the one-dimensional umbrella sampling at other values of R_{ee} leads to the second free-energy profile shown in Fig. 1(b). Although the additional sampling has moved the transition to slightly larger R_{ee} , the relative change is small, suggesting that 1D sampling is sufficient to obtain a reasonably accurate representation of the free-energy landscape.

We can also use our computed free-energy landscapes to help understand the response of the nanotube if a compressive force is applied along the end-to-end vector. For a macroscopic rod, Euler buckling predicts that the rod will remain straight until a critical

force is reached, namely $F_E = k_B T L_p \pi^2 / L_c^2$ where L_p and L_c are the persistence and contour lengths, respectively. However, it is well known that in microscopic systems this instability is rounded by thermal fluctuations with the transition becoming less sharp as L_c/L_p increases.⁷¹ For the current example $L_p/L_c \approx 20$, so the transition is expected to be quite sharp.

In Fig. 3(a) we show how the free-energy landscape depends on force and in Fig. 3(b) we plot $F(R_{ee}) = -dA(R_{ee})/dR_{ee}$ for both the computed landscape and the WLC fit. In line with the expectations outlined above, at $F \approx F_E = 2.51$ pN the section of the landscape associated with homogeneous bending becomes very flat and R_{ee} decreases rapidly with increasing force.

The other major feature is that the kinked state becomes a free-energy minimum as the force is increased. At $F = F_{\text{kink}} = 2.08$ pN the free-energy minima associated with the kinked ($R_{ee} = 54$ nm) and unkinked ($R_{ee} = 323$ nm) states are degenerate separated by a barrier of $20.3 k_B T$; at equilibrium a transition to the kinked state would be expected at this force. At forces just above F_E the kinked nanotube becomes the only stable state. Similarly, the plot of $F(R_{ee})$ has an unstable region of positive slope at R_{ee} values associated with the crossover between the kinked and unkinked states, and at F_{kink} a Maxwell-like equal area rule applies in Fig. 3(b).

The closest experimental realization of the above is the force-induced bending of DNA origami that has been achieved by single-stranded tethers that connect different parts of the origami. This approach has been used to bend six-helix bundles³² and cuboidal origami rods,³³ where the degree of bending can be controlled by the length of the tether. However, in these examples, the forces exerted by the single-stranded tethers, rather than taking a constant value, also depend on the end-to-end distance.

Comparing the free-energy landscapes of the three designs that we consider (Fig. 1 and 4), although they all show the same basic behaviour, there are also significant variations between them. Design 1 is actually not an origami, but a single-stranded tile structure that is built from just six repeating 42-bp strands.⁶⁵ More important than the absence of a scaffold strand for the current study is that all the junctions are single crossovers (i.e. just one strand crosses between the adjacent helices) as this potentially allows significantly more freedom of motion at the junctions in response to stress. Design 2 is an experimentally-realized origami^{68,69} that involves a majority of double crossovers. Notably, the scaffold crossovers are located very close to staple crossovers, with small 2-bp domains separating them; the dissociation of these 2-bp sections can lead to significantly increased local flexibility. Design 3 was constructed as a contrast to design 2 with the aim of increasing the mechanical strength. In this origami all crossovers are mediated by staples and all are double crossovers. All nicks are placed midway between junctions meaning the shortest domain is 7 bp; this also leads to planes where every helix has either a junction or a nick, which are likely to be preferred sites for local bending.

The persistence lengths obtained from the WLC fits for designs 1 and 2 are $6.5 \mu\text{m}$ and $5.3 \mu\text{m}$; these agree with the values extracted from the thermal fluctuations of the nanotubes in unbiased simulations.⁵⁷ However, they are higher than the experi-

mental values of $3.3 \mu\text{m}$ ⁶⁵ and $2.4 \mu\text{m}$ ⁶⁸. We note that for design 1, there was a significant dispersion of persistence lengths ($1.6 \mu\text{m}$ to $4.7 \mu\text{m}$) between the individual nanotubes probed in the experiments, which was attributed to structural differences among different nanotubes⁶⁵. Experimental persistence length have also been found to depend on the post-assembly treatment of the origamis.³² This suggests that the experiments are measuring the persistence lengths of a heterogeneous ensemble of nanotubes that include some with structural defects that lower the persistence length. By contrast, the simulations measure the persistence length of a perfectly assembled nanotube. That oxDNA overestimates the stretch modulus may also contribute to this difference.⁵⁷

The persistence lengths of designs 1 and 3 are very similar, but for design 2 it is lower by about 20%. If one inspects the number of intact base pairs as a function of R_{ee} (Fig. S8), there is a noticeable difference between the designs; while for designs 1 and 3 there are no significant changes until the onset of kinking, for design 2 there is a small but noticeable decrease. Inspection of snapshots of design 2 reveals that the short 2-bp domains noted above are occasionally broken; this is probably one reason for this nanotube's greater flexibility—the less regular distribution of crossovers may also play a role.

Design 1 shows a clear change of slope of the free-energy landscape associated with kinking. However, the deviation from the worm-like chain fit is more gradual for the two origamis and starts to occur prior to clear kink formation (see the example configurations in Figs. S6 and S7 and the energetic and structural descriptors in Figs. S8 and S9). For example, for design 3, R_{ee} has to be significantly less than 100 nm for a kink to appear, even though deviations from the worm-like chain fit start to appear at about 150 nm. This non-linear elasticity is because the nanotubes exploit the heterogeneity of their local mechanical properties to partially localize stronger bending at mechanically more flexible regions.

The kinks in the nanotubes look somewhat like the kinks in a macroscopic tube. The cross-sections become flattened and wider, but the detailed structure depends on the nanotube design, the main difference being how the tubes respond to the compressive stresses on the inside of the kink. The single crossovers in design 1 mean the helical sections have the most freedom to reorient, just through loss of the coaxial stacking interactions at the junction and perhaps some fraying of adjacent base pairs. In the example in Fig. 1(d) this allows the outer two helices in the inside of the kink to splay out, and in the (orange) middle helix a section is oriented almost perpendicular to the nanotube axis. By contrast the three helices on the outside of the kink are almost co-planar and bend continuously around the kink.

In design 2, this freedom of motion is achieved by the loss of base pairs, particularly associated with the short 2-bp domains already mentioned, but also by the unbinding of short staple end-domains. In design 3, the helical sections are most constrained, because of the exclusively double crossovers and the lack of short staple domains. Kinking occurs at the planes of nicks and junctions by the loss of coaxial stacking, but the free-energetic advantage of kinking rather than homogeneously bending is least for

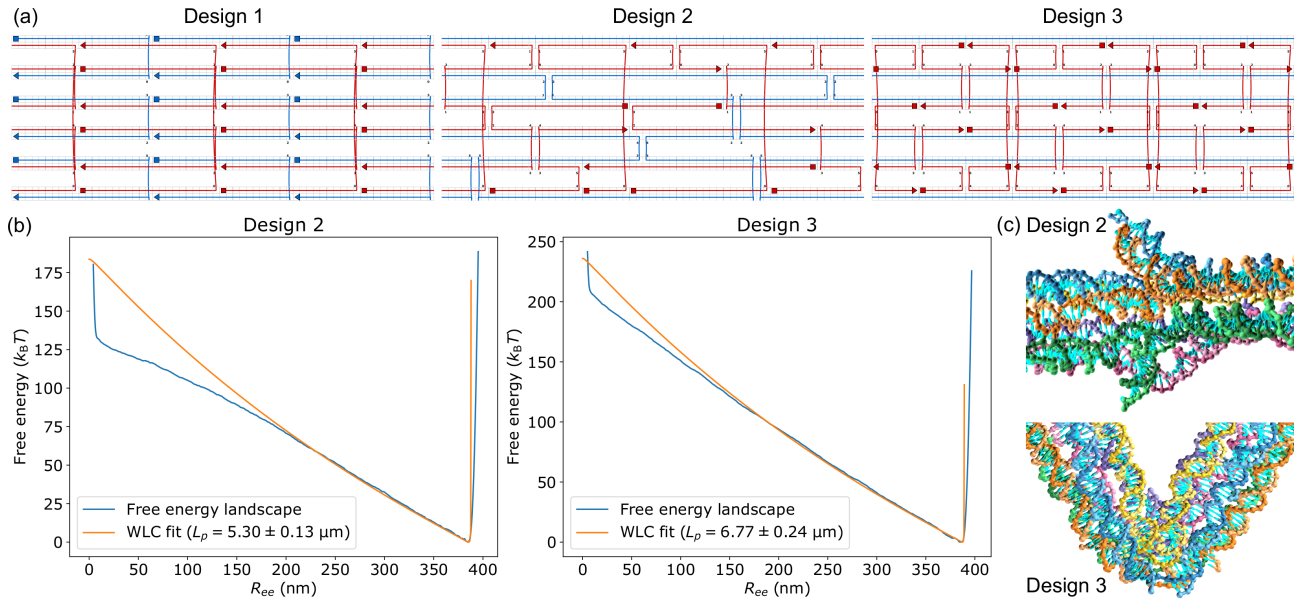


Fig. 4 (a) Strand routing diagrams for sections of the three nanotube designs as represented in caDNAno.⁷² For designs 1 and 3 the pattern repeats along the nanotube. For the origamis (designs 2 and 3), the scaffold is in blue and staples in red. (b) Free-energy landscapes of designs 2 and 3 as a function of R_{ee} . (c) Close-up views (from the inside and side-on) of kinks for design 2 and 3 configurations with $R_{ee} = 92$ nm and 54 nm, respectively. Further configurations of the two nanotubes are depicted in Figs. S6 and S7.

this system. The design has significantly increased the nanotube's stiffness and strength with respect to extreme bending compared to design 2.

The increased resistance to kinking also leads to differences in the predicted behaviour when a compressive force is applied along the end-to-end vector compared to design 1 (Fig. S10). For design 2, the kinked state becomes equal in free energy to the unkinked state only very close to the Euler buckling critical force, whereas for design 3 the force-dependent free-energy landscape only ever has a single free-energy minimum and the nanotube is instead predicted to transition continuously between unkinked and kinked states.

It is also of interest to test whether extreme bending leads to any irreversible damage to the nanotubes. One reason for irreversibility would be if the stresses lead to staple dissociation, but such events were never seen in any of our simulations. To explore this further, we took configurations from the most bent umbrella sampling windows, and used them as starting points in unbiased molecular dynamics simulations. The time evolution of the end-to-end distance is shown in Fig. 5 for all three designs. All were able to relax back to their equilibrium R_{ee} value. Furthermore, after they have fully relaxed, the number of pairs of interactions is essentially the same as that of a normal unstressed nanotube (Table S1). This result suggests that strong bending and kink formation do not induce irreversible structural changes to the nanotubes. This reversibility is because, on the time scales of our simulations, the structural disruption caused by the extreme bending stresses involves at most only partial melting of the staples rather than complete dissociation.

The effects of the design differences are also evident from these simulations. In particular, for design 2 the slow reannealing of broken base pairs, especially at the site of the kink, led to a slower

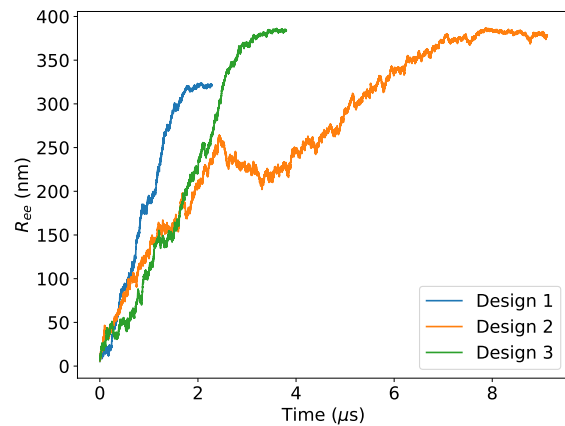


Fig. 5 Time evolution of R_{ee} in unbiased molecular dynamics simulations that start from nanotube configurations with R_{ee} close to zero that were generated in our umbrella sampling simulations. All are able to relax back to their equilibrium state. Movies of these trajectories are included as Supplementary Information.

recovery of the equilibrium structure.

3.1.1 DNA nanotube stretching

The form of the free-energy landscape at R_{ee} values beyond the minimum contains information about the stretching of the nanotubes. In particular, the force-extension curve of the nanotube can be extracted from $A(R_{ee})$ (as detailed in the Supplementary Information); then by fitting this curve to that for an extensible WLC the stretch modulus can be obtained.⁷³ The resulting force-extension curve and the fit to it are shown in Fig. 6 for design 1 and in Fig. S11 for the other two designs. All designs give a

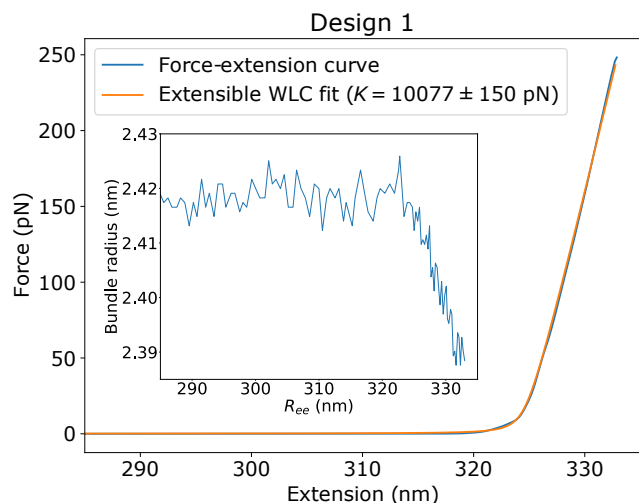


Fig. 6 Force-extension curve for the design 1 nanotube along with the extensible WLC fit (see Table S3 for the fit parameters). The inset shows the average nanotube radius as a function of R_{ee} .

value of the extensional modulus that is roughly 10 000 pN. This is significantly less than the six times the oxDNA extensional modulus for double-stranded DNA (2700 pN) that one might have expected. The reason is that the nanotube can be extended not only by the stretching of the individual helices, but also by a straightening of the helices within the origami structure. It is well evidenced that the helices in a relaxed origami are not perfectly parallel, but splay out by a small angle at each junction.^{3,20,58} Reduction of this angle will cause a reduction in the interhelix distance and hence the nanotube radius. Such a reduction in the nanotube radius is clearly seen in the stretching regime, whereas it is roughly constant in the regime associated with homogeneous bending (Fig. 6 inset).

3.2 Twisted DNA origami sheets

As mentioned in the introduction, when an inextensible sheet is twisted there is an inevitable coupling to bending, as is illustrated for an A4 sheet of paper in Supplementary Fig. S12. However, the curvature that results can be of either sign. In the limit that this curvature is localized at a line (i.e. a fold), the two states correspond to a “valley” fold about one diagonal or a “mountain” fold about the opposite diagonal.

Does a similar picture hold for a twisted 2D origami sheet? Although such origamis are not inextensible, the bending modulus perpendicular to the directions of the helices is expected to be relatively low. For example, it was not possible to get a well-defined cryo-EM structure for a 2D origami sheet because the fluctuations were so large.⁶ Furthermore, SAXS experiments suggest that twisted sheets exhibit significant curvature, with CanDo^{17,18} modelling predicting that the curvature increases with twist.⁵⁸

Because there is no difference between the two sides of a paper sheet, the two states for the twisted sheet are equivalent. By contrast, the two faces of a chiral DNA origami sheet are inequivalent. However, it is not yet known whether both states are possible for an origami sheet, or whether instead one is overwhelmingly

favoured? For example, the SAXS measurements are not sensitive to the sign of the curvature. AFM studies have attempted to infer the preferred curvature based on the assumption that the origami are more likely to bind to the surface when they land convex face down.^{35,59}

We first explored these questions for a 2D origami sheet with a Rothemund-like design; such single-layer origamis are right-twisted because the junction spacing in the design would require a DNA pitch length of 10.67 base pairs to be flat; this is larger than the natural pitch length of about 10.5 base pairs. On relaxing the initial flat configuration generated from converting the caDNAno design, the origami twisted and rolled up as expected (this effect has been seen before for oxDNA⁵¹). However, when we repeated this relaxation multiple times, the resulting structures exhibited both curvatures. These results indicated that both forms are free-energy minima and that the initial flat geometry is in the transition region with stochastic effects during the relaxation causing the system to fall into one or other of the two basins.

To characterize this bistability further we computed the free-energy landscape of the 2D origami sheet as a function of two order parameters, namely the two diagonal distances R_1 and R_2 that are shown in Fig. 7(a). This was again achieved using umbrella sampling with each individual simulation centred around a different grid point in the 2D order parameter space.

The resulting free-energy landscape is shown in Fig. 7(b). The landscape has two free-energy minima and is roughly symmetric about the diagonal $R_1 = R_2$. For each free-energy minimum one diagonal distance is roughly unperturbed (with a value of about 80 nm) whilst the other diagonal distance is reduced by about 40% due to the curvature. The free-energy minima are also very asymmetric with the soft mode corresponding to changing the degree of curvature perpendicular to the “unperturbed diagonal”.

Inspection of the configurations associated with the two free-energy minima confirms that both have a right-handed twist but that they have opposite curvatures. Quantitative confirmation comes from the plots of the mean curvature in Fig. 7(d). The mean curvature for the two forms is always positive or negative, respectively, with the pattern of local variation showing an approximate symmetry with respect to the relevant diagonal.

There is a small free-energy difference between the two minima of $3.5k_B T$. Although there is no reason to expect the two free-energy minima to be degenerate because they are not equivalent by symmetry, the physical reason why the positive curvature form is slightly more stable is not clear. The free-energy barrier (measured with respect to the more stable form) is $7.5k_B T$. Although this barrier is sufficiently high that transitions would be unlikely to be seen in unbiased simulations, on typical experimental time scales both forms would likely be sampled.

The free-energy transition state occurs near to the $R_1 = R_2$ diagonal at $(R_1, R_2) = (68 \text{ nm}, 72 \text{ nm})$, but slightly displaced towards the higher free-energy minimum. It is not a flat sheet but corresponds to a more saddle-like configuration that retains the twist but has an overall mean curvature that is close to zero.

The second example that we have considered is a twisted two-layer origami based upon a square lattice of helices. As ob-

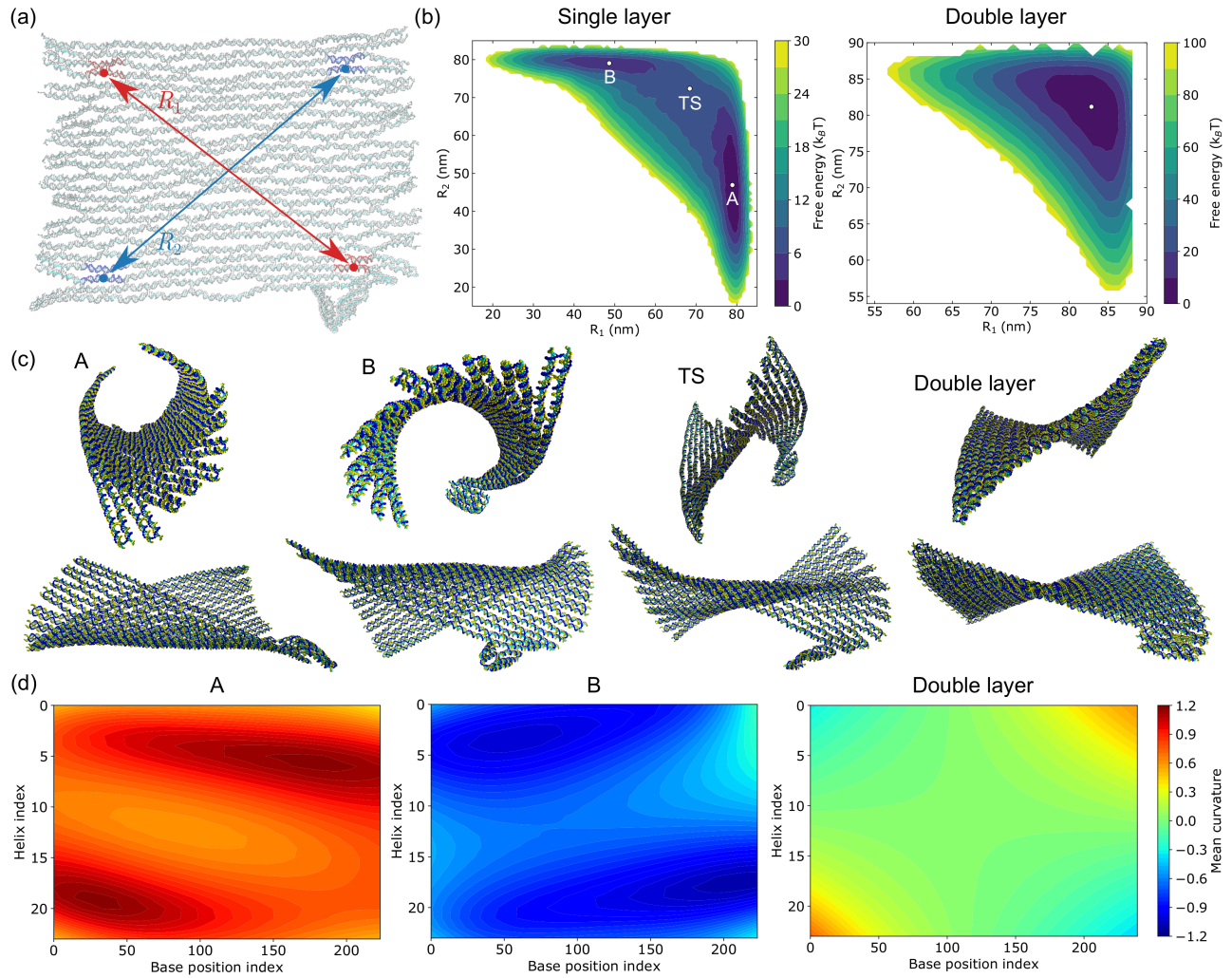


Fig. 7 (a) The two diagonal distances R_1 and R_2 that are used as order parameters in the umbrella sampling illustrated for a flat configuration of the single-layer sheet. The additional short helices in the bottom right corner are to aid identification of the orientation of the origami. Positive curvature corresponds to the edges of the sheet being curved up out of the plane. (b) Free-energy landscapes of the single-layer and double-layer twisted sheets. (c) End-on and side-on views of the configurations associated with the two free-energy minima and the transition state (TS) of the single-layer sheet, and with the free-energy minimum of the double-layer sheet. (d) Mean curvature (the average of the principal curvatures) of configurations at the two free-energy minima of the single-layer sheet and the free-energy minimum of the double-layer sheet as a function of the base-pair position within the sheet.

served experimentally,⁷⁴ this second layer significantly increases the stiffness of the origami compared to the single-layer designs; in particular we expect the sheet to be much stiffer with respect to bending perpendicular to the helix axis, as bending is now coupled to the stretching and compression of the inter-helix bonds on the outside and inside of the bend, respectively.

The free-energy landscape of the twisted two-layer origami is quite different from the single-layer origami. It has a single free-energy minimum with $R_1 \approx R_2$. The increased bending stiffness has removed the bistability that is observed for the single-layer origami. A saddle-like geometry, which was characteristic of the transition region in Fig. 7(b), is now lowest in free energy, as also predicted by CanDo.⁷⁴ In this geometry much of the stress due to twist is accommodated through stretching and compression of the origami rather than just by bending. Reflecting the origami's greater stiffness, the free energy increases much more rapidly on

moving away from the minimum. Hence, the magnitude of the structural fluctuations will be much less than for a single-layer origami sheet.

The mean curvature for a perfect saddle would be zero due to the cancellation of the negative and positive curvatures along the two diagonals. Although not exactly zero, the mean curvature for the two layer origami is close to zero over the whole origami except for very close to the corners. The Gaussian curvature (the product of the principle curvatures), by contrast would be expected to be uniformly negative, as it is, except again at the corners (Fig. S13).

4 Conclusions

We have shown that it is feasible to compute the free-energy landscapes associated with the mechanical deformation of large DNA nanostructures, such as DNA origami, when described with a

nucleotide-level coarse-grained model. The use of umbrella sampling with many windows allows all parts of the free-energy landscapes to be sampled in a highly parallel manner.

The first example that we considered is the extreme bending of DNA nanotubes, for which we compute the free-energy landscape as a function of an end-to-end distance. Such nanotubes are extremely stiff and are promising building blocks for nanoscale engineering. In the homogeneous bending regime, the behaviour is well described by the worm-like chain model. In the extreme bending regime the bending stress localizes at one or two kinks, where the ease of kinking and the nature of the deformations at the kink depends sensitively on the local features of the nanotube design. Importantly, the nanotubes can also reversibly recover from this kinking when the stress is removed. The landscapes at end-to-end distances larger than the nanotube's relaxed length also allows us to extract the stretch modulus of the nanotubes. Their values are somewhat less than would be expected for six helices stretched in parallel, because the nanotubes can also respond to the tension by reducing their radius.

We have also characterized the free-energy landscapes of twisted DNA origami sheets. For a single-layer sheet there are two nearly degenerate free-energy minima because of the strong coupling of the twist to the soft bending mode perpendicular to the helices with the two minima having opposite curvature. This bistability disappears for a twisted two-layer DNA origami; the stiffening of the bending mode means that the preferred form has a saddle-like geometry where the twist stress is also accommodated through stretching and compression of the sheet.

In order for it to be feasible to compute free-energy landscapes for DNA origamis using the current approach it is important that the properties of the systems vary relatively continuously as the order parameters change, so that equilibration within each umbrella sampling window can be relatively rapid. Such calculations becomes more problematic when discontinuous changes occur. We saw this for the kinking transition in the nanotubes, where to more accurately locate the transition we needed to introduce a second order parameter that provided a more continuous pathway between the kinked and unkinked states. Thus, the approach can be most easily applied to landscapes associated with mechanical deformations and could be applied to larger multi-origami systems in such cases. By contrast, calculating free-energy landscapes that involve significant assembly or disassembly, although feasible for small and medium-sized^{46–51} DNA systems, is likely to be computationally very challenging for systems of the size of DNA origamis.

As well as being used to explore the fundamental mechanical properties of DNA origami, we expect the current methods to find application in DNA mechanotechnology²⁷ where DNA origami systems are increasingly being used as part of force-sensing²⁸ or force-applying²⁹ devices, and an accurate characterization of the compliance of the origami devices under the relevant mechanical loads is likely to be important for their calibration. Accurate characterization of origami mechanics is also likely to be important for understanding stress accumulation in the self-assembly of origamis into higher-order structures, be it an unwanted side effect which hinders correct assembly, or a design strategy to con-

trol and direct the assembly.^{38,39}

Author Contributions

CKW extended the oxDNA simulation code to allow umbrella sampling on the relevant coordinates. CKW performed and analysed the simulations on the nanotubes. CT, CKW and JS performed and analysed the simulations on the two-dimensional sheets. CKW and JPKD wrote the paper.

Conflicts of interest

There are no conflicts to declare.

Acknowledgements

CKW is grateful to the Croucher Foundation for financial support. The authors acknowledge the use of the University of Oxford Advanced Research Computing (ARC) facility (<http://dx.doi.org/10.5281/zenodo.22558>) and the resources provided by the Cambridge Service for Data Driven Discovery (CSD3). We are grateful to the group of Christoph Wälti for helpful discussions.

References

- 1 F. Hong, F. Zhang, Y. Liu and H. Yan, *Chem. Rev.*, 2017, **117**, 12584–12640.
- 2 N. C. Seeman and H. F. Sleiman, *Nat. Rev. Mater.*, 2017, **3**, 17068.
- 3 P. W. K. Rothmund, *Nature*, 2006, **440**, 297–302.
- 4 S. Dey, C. Fan, K. V. Gothelf, J. Li, C. Lin, L. Liu, N. Liu, M. A. D. Nijenhuis, B. Sacca, F. C. Simmel, H. Yan and P. Zhan, *Nat. Rev. Methods Primers*, 2021, **1**, 13.
- 5 X.-C. Bai, T. G. Martin, S. H. W. Scheres and H. Dietz, *Proc. Natl. Acad. Sci. U. S. A.*, 2012, **109**, 20012–20017.
- 6 M. Kube, F. Kohler, E. Feigl, B. Nagel-Yüksel, E. M. Willner, J. J. Funke, T. Gerlin, P. Stömmel, M. N. Honemann, T. G. Martin, S. H. W. Scheres and H. Dietz, *Nat. Commun.*, 2020, **11**, 6229.
- 7 J. Yoo and A. Aksimentiev, *Proc. Natl. Acad. Sci. U. S. A.*, 2013, **110**, 20099–20104.
- 8 C.-Y. Li, E. A. Hemmig, J. Kong, J. Yoo, S. Hernández-Ainsa, U. F. Keyser and A. Aksimentiev, *ACS Nano*, 2015, **9**, 1420–1433.
- 9 K. Göpfrich, C.-Y. Li, M. Ricci, S. P. Bhamidimarri, J. Yoo, B. Gyenes, A. Ohmann, M. Winterhalter, A. Aksimentiev and U. F. Keyser, *ACS Nano*, 2016, **10**, 8207–8214.
- 10 C. Maffeo, J. Yoo and A. Aksimentiev, *Nucleic Acids Res.*, 2016, **44**, 3013–3019.
- 11 S. M. Slone, C.-Y. Li, J. Yoo and A. Aksimentiev, *New J. Phys.*, 2016, **18**, 055012.
- 12 C. Lee, J. Y. Lee and D.-N. Kim, *Nat. Commun.*, 2017, **8**, 2067.
- 13 T. E. Ouldridge, A. A. Louis and J. P. K. Doye, *J. Chem. Phys.*, 2011, **134**, 085101.
- 14 P. Šulc, F. Romano, T. E. Ouldridge, L. Rovigatti, J. P. K. Doye and A. A. Louis, *J. Chem. Phys.*, 2012, **137**, 135101.
- 15 B. E. K. Snodin, F. Randisi, M. Mosayebi, P. Šulc, J. S. Schreck,

- F. Romano, T. E. Ouldrige, R. Tsukanov, E. Nir, A. A. Louis and J. P. K. Doye, *J. Chem. Phys.*, 2015, **142**, 234901.
- 16 C. Maffeo and A. Aksimentiev, *Nucleic Acids Res.*, 2020, **48**, 5135–5146.
 - 17 D.-N. Kim, F. Kilchherr, H. Dietz and M. Bathe, *Nucleic Acids Res.*, 2011, **40**, 2862–2868.
 - 18 C. E. Castro, F. Kilchherr, D.-N. Kim, E. L. Shiao, T. Wauer, P. Wortmann, M. Bathe and H. Dietz, *Nat. Methods*, 2011, **8**, 221–229.
 - 19 J. Y. Lee, J. G. Lee, C. Lee, Y.-J. Kim, K. S. Kim, T. H. Kim and D.-N. Kim, *ACS Nano*, 2021, **15**, 1002–1015.
 - 20 B. E. K. Snodin, J. S. Schreck, F. Romano, A. A. Louis and J. P. K. Doye, *Nucleic Acids Res.*, 2019, **47**, 1585–1597.
 - 21 J. F. Berengut, J. C. Berengut, J. P. K. Doye, D. Prešern, A. Kawamoto, J. Ruan, M. J. Wainwright and L. K. Lee, *Nucleic Acids Res.*, 2019, **47**, 11963–11975.
 - 22 R. Sharma, J. S. Schreck, F. Romano, A. A. Louis and J. P. K. Doye, *ACS Nano*, 2017, **11**, 12426–12435.
 - 23 Z. Shi, C. E. Castro and G. Arya, *ACS Nano*, 2017, **11**, 4617–4630.
 - 24 L. Zhou, A. E. Marras, C.-M. Huang, C. E. Castro and H.-J. Su, *Small*, 2018, **14**, 1802580.
 - 25 C.-M. Huang, A. Kucinic, J. V. Le, C. E. Castro and H.-J. Su, *Nanoscale*, 2019, **11**, 1647–1660.
 - 26 Z. Shi and G. Arya, *Nucleic Acids Res.*, 2019, **48**, 548–560.
 - 27 A. T. Blanchard and K. Salaita, *Science*, 2019, **365**, 1080–1081.
 - 28 P. K. Dutta, Y. Zhang, A. T. Blanchard, C. Ge, M. Rushdi, K. Weiss, C. Zhu, Y. Ke and K. Salaita, *Nano Lett.*, 2018, **18**, 4803–4811.
 - 29 P. C. Nickels, B. Wünsch, P. Holzmeister, W. Bae, L. M. Kneer, D. Grohmann, P. Tinnefeld and T. Liedl, *Science*, 2016, **354**, 305–307.
 - 30 Y. Wang, J. V. Le, K. Crocker, M. A. Darcy, P. D. Halley, D. Zhao, N. Andrioff, C. Croy, M. G. Poirier, R. Bundschuh and C. Castro, *Nucleic Acids Res.*, 2021, Advance Article gkab656.
 - 31 H. Dietz, S. M. Douglas and W. M. Shih, *Science*, 2009, **325**, 725–730.
 - 32 T. Liedl, B. Högberg, J. Tytell, D. E. Ingber and W. M. Shih, *Nat. Nanotechnol.*, 2010, **5**, 520–524.
 - 33 L. Zhou, A. E. Marras and C. E. Castro, *ACS Nano*, 2014, **8**, 27–34.
 - 34 F. Gür, S. Kempter, F. Schueder, C. Sikeler, M. J. Urban, R. Jungmann, P. C. Nickels and T. Liedl, *Adv. Mater.*, 2021, Early View 2101986.
 - 35 A. C. Stammers, *PhD thesis*, University of Leeds, 2018.
 - 36 L. Zhou, A. E. Marras, H.-J. Su and C. E. Castro, *Nano Lett.*, 2015, **15**, 1815–1821.
 - 37 P. Shrestha, T. Emura, D. Koirala, Y. Cui, K. Hidaka, W. J. Maximuck, M. Endo, H. Sugiyama and H. Mao, *Nucleic Acids Res.*, 2016, **44**, 6574–6582.
 - 38 J. F. Berengut, C. K. Wong, J. C. Berengut, J. P. K. Doye, T. E. Ouldrige and L. K. Lee, *ACS Nano*, 2020, **14**, 17428–17441.
 - 39 M. F. Hagan and G. M. Grason, *Rev. Mod. Phys.*, 2021, **93**, 025008.
 - 40 G. Torrie and J. Valleau, *J. Comput. Phys.*, 1977, **23**, 187–199.
 - 41 C. Maffeo, B. Luan and A. Aksimentiev, *Nucleic Acids Res.*, 2012, **40**, 3812–3821.
 - 42 F. Häse and M. Zacharias, *Nucleic Acids Res.*, 2016, **44**, 7100–7108.
 - 43 H. Kang, J. Yoo, B.-K. Sohn, S.-W. Lee, H. S. Lee, W. Ma, J.-M. Kee, A. Aksimentiev and H. Kim, *Nucleic Acids Res.*, 2018, **46**, 9401–9413.
 - 44 R. Cortini, X. Cheng and J. C. Smith, *J. Phys.: Condens. Matter*, 2017, **29**, 084002.
 - 45 K. Liebl and M. Zacharias, *J. Phys. Chem. B*, 2017, **121**, 11019–11030.
 - 46 R. M. Harrison, F. Romano, T. E. Ouldrige, A. A. Louis and J. P. K. Doye, *J. Chem. Theory Comput.*, 2019, **15**, 4660–4672.
 - 47 M. Mosayebi, A. A. Louis, J. P. K. Doye and T. E. Ouldrige, *ACS Nano*, 2015, **9**, 11993–12003.
 - 48 F. Romano, D. Chakraborty, J. P. K. Doye, T. E. Ouldrige and A. A. Louis, *J. Chem. Phys.*, 2013, **138**, 085101.
 - 49 T. E. Ouldrige, A. A. Louis and J. P. K. Doye, *Phys. Rev. Lett.*, 2010, **104**, 178101.
 - 50 T. E. Ouldrige, R. L. Hoare, A. A. Louis, J. P. K. Doye, J. Bath and A. J. Turberfield, *ACS Nano*, 2013, **7**, 2479–2490.
 - 51 D. C. Khara, J. S. Schreck, T. E. Tomov, T. E. Ouldrige, J. P. K. Doye and E. Nir, *Nucleic Acids Res.*, 2018, **46**, 1553–1561.
 - 52 W. Pfeifer and B. Saccà, *Biol. Chem.*, 2018, **399**, 773–785.
 - 53 C. Bustamante, J. F. Marko, E. D. Siggia and S. B. Smith, *Science*, 1994, **265**, 1599–1600.
 - 54 R. Vafabakhsh and T. Ha, *Science*, 2012, **337**, 1097–1101.
 - 55 J. S. Mitchell, C. A. Laughton and S. A. Harris, *Nucleic Acids Res.*, 2011, **39**, 3928–3938.
 - 56 R. M. Harrison, F. Romano, T. E. Ouldrige, A. A. Louis and J. P. K. Doye, *Coarse-Grained Modelling of Strong DNA Bending I: Thermodynamics and Comparison to an Experimental “Molecular Vice”*, 2015, <https://arxiv.org/abs/1506.09005>.
 - 57 H. Chhabra, G. Mishra, Y. Cao, D. Prešern, E. Skoruppa, M. M. C. Tortora and J. P. K. Doye, *J. Chem. Theory Comput.*, 2020, **16**, 7748–7763.
 - 58 M. A. B. Baker, A. J. Tuckwell, J. F. Berengut, J. Bath, F. Benn, A. P. Duff, A. E. Whitten, K. E. Dunn, R. M. Hynson, A. J. Turberfield and L. K. Lee, *ACS Nano*, 2018, **12**, 5791–5799.
 - 59 A. N. Marchi, I. Saaem, B. N. Vogen, S. Brown and T. H. LaBean, *Nano Lett.*, 2014, **14**, 5740–5747.
 - 60 J. P. K. Doye, T. E. Ouldrige, A. A. Louis, F. Romano, P. Šulc, C. Matek, B. E. K. Snodin, L. Rovigatti, J. S. Schreck, R. M. Harrison and W. P. J. Smith, *Phys. Chem. Chem. Phys.*, 2013, **15**, 20395–20414.
 - 61 E. Benson, A. Mohammed, D. Rayneau-Kirkhope, A. Gådin, P. Orponen and B. Högberg, *ACS Nano*, 2018, **12**, 9291–9299.
 - 62 C. Maffeo, R. Schöpflin, H. Brutzer, A. Stehr, R. and Aksimentiev, G. Wedemann and R. Seidel, *Phys. Rev. Lett.*, 2010, **105**, 158101.
 - 63 L. Rovigatti, P. Šulc, I. Z. Regulý and F. Romano, *J. Comput. Chem.*, 2015, **36**, 1–8.

- 64 S. Kumar, J. M. Rosenberg, D. Bouzida, R. H. Swendsen and P. A. Kollman, *J. Comput. Chem.*, 1992, **13**, 1011–1021.
- 65 D. Schiffels, T. Liedl and D. K. Fygenson, *ACS Nano*, 2013, **7**, 6700–6710.
- 66 D. J. Kauert, T. Kurth, T. Liedl and R. Seidel, *Nano Lett.*, 2011, **11**, 5558–5563.
- 67 C. Lee, K. S. Kim, Y.-J. Kim, J. Y. Lee and D.-N. Kim, *ACS Nano*, 2019, **13**, 8329–8336.
- 68 M. Siavashpouri, C. H. Wachauf, M. J. Zakhary, F. Praetorius, H. Dietz and Z. Dogic, *Nat. Mater.*, 2017, **16**, 849–856.
- 69 E. Pfitzner, C. Wachauf, F. Kilchherr, B. Pelz, W. M. Shih, M. Rief and H. Dietz, *Angew. Chem. Int. Ed.*, 2013, **52**, 7766–7771.
- 70 N. B. Becker, A. Rosa and R. Everaers, *Eur. Phys. J. E*, 2010, **32**, 53–69.
- 71 E. Pilyugina, B. Krajina, A. J. Spakowitz and J. D. Schieber, *Polymer*, 2017, **9**, 99.
- 72 S. M. Douglas, A. H. Marblestone, S. Teerapittayanon, A. Vazquez, G. M. Church and W. M. Shih, *Nucleic Acids Res.*, 2009, **37**, 5001–5006.
- 73 T. Odijk, *Macromolecules*, 1995, **28**, 7016–7018.
- 74 Y. Zhang, F. Li, X. Mao, M. Li and X. Zuo, *ACS Appl. Bio Mater.*, 2020, **3**, 2610–2616.